buildings

MDPI

*Article*

# Analysis of Post-Construction Settlement of Pile-Supported Geosynthetic-Reinforced Embankment

**Chaochao Sun [1,2,†], Jili Qu [1,*,†], Yabo Shi [3], Guangping Li [1,†], Longlong Wei [1,2,†], Xiangyu Zhang [1,2,†], Xiaodong Yang [4,†], Dongmei Chen [1,†], Huanqing Liu [1] and Shiguo Xu [5]**

[1] School of Civil Engineering, Kashi University, Kashi 844000, China; scc19890325@ksu.edu.cn (C.S.); 13279735359@163.com (G.L.); 13679463067@163.com (L.W.); 18055430944@163.com (X.Z.); 18899355826@163.com (D.C.); 18238560719@163.com (H.L.)
[2] Xinjiang Key Laboratory of Engineering Materials and Structural Safety, Kashi 844000, China
[3] College of Civil Engineering and Architecture, Henan University of Technology, Zhengzhou 450001, China; 13837565087@163.com
[4] School of Transportation, Kashi University, Kashi 844000, China; 18709982512@163.com
[5] School of Infrastructure Engineering, Dalian University of Technology, Dalian 116024, China; sgxu@dlut.edu.cn
* Correspondence: qujiliqwq@163.com
† Current address: College of Civil Engineering, Kashi University, Kashi 844000, China.

**Abstract**

Pile-supported geosynthetic-reinforced embankments, as effective foundation improvements, are being used increasingly often in the construction of highway and railway engineering at present. The geosynthetic-reinforced load transfer platform in the horizontal direction was simulated to the thin plate, and then the differential equation of the curved surface and the nonlinear foundation model were used to solve the analytical expression of the post-construction settlement of the reinforced area, and the engineering example was used to verify it. Furthermore, a finite element model was developed to simulate the settlement. The analysis utilized a static general step and incorporated a linear elastic–perfectly plastic model with the Mohr–Coulomb failure criterion. The numerical result of 19.7 mm was consistent with the theoretical prediction of 20.1 mm, demonstrating a mere 2.0% relative error and substantiating the validity and accuracy of the theoretical model. The analysis examined how bending stiffness, the subgrade reaction coefficient, pile spacing, and embankment height affect post-construction settlement. The results demonstrate that the settlement increases with larger pile spacings or lower values of the subgrade reaction coefficient and bending stiffness. Notably, the settlement increases with embankment height only until a critical height—calculated from the bearing capacity of the inter-pile soil—is exceeded. Based on this, it was found that the subgrade reaction coefficient was identified as the most influential parameter, followed by pile spacing and then bending stiffness. These findings lead to practical recommendations for engineering practice.

**Keywords:** pile-supported geogrid-reinforced platform; nonlinear foundation model; post-construction settlement; finite element analysis; affect; practical recommendations



Academic Editor: Giuseppina Uva

Received: 25 February 2026
Revised: 3 April 2026
Accepted: 13 April 2026
Published: 16 April 2026



## 1. Introduction

The pile-supported reinforced embankment method refers to a ground improvement system that combines vertical piles with a horizontal reinforced composite load transfer platform, thereby effectively supporting the loads imposed by the upper embankment [1–6] (as shown in Figure 1).

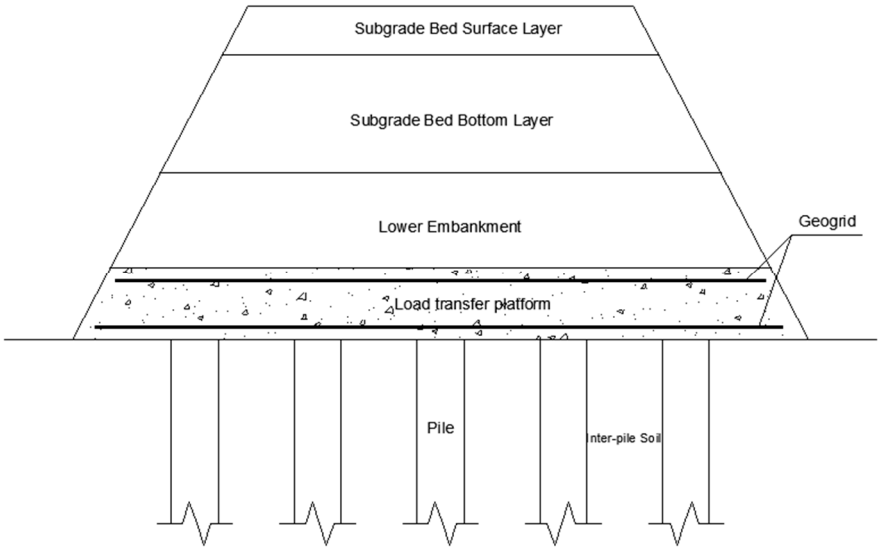


**Figure 1.** The schematic diagram of pile-supported geosynthetic-reinforced embankment.

The pile-supported geosynthetic-reinforced embankment technique offers significant advantages, including high bearing capacity, minimal settlement, and cost-effectiveness [7–10]. It has been successfully employed in domestic and international projects such as highway widening, airport runway embankments, and ground improvement for bridge approaches on soft foundations [11–14]. Compared to other ground improvement technologies, this method demonstrates broad application prospects. Currently, it is widely adopted in regions such as the southeastern coastal areas of China, cities with numerous inland lakes, and the Pearl River Delta region [15,16].

Zhang et al. [17] analyzed the load transfer mechanism among geosynthetics, piles, and inter-pile soil under embankment loading, establishing a foundation stress model and proposing a finite difference solution for the pile–soil stress ratio. Zheng et al. [18], considering the force exerted by horizontal reinforcement on the pile heads, derived an analytical expression for the pile–soil stress ratio in pile-supported reinforced embankments. Zhao et al. [19], based on the Winkler elastic foundation circular plate theory, developed a deflection function for the horizontal reinforcement and subsequently formulated a calculation method for the pile–soil stress ratio. In another study, Zhao et al. [20] treated the geocell as a thin plate with small deflection. Assuming coordinated deformation between the geocell and the improved zone based on the Winkler foundation model, and considering the lateral friction at the soil-reinforcement interface, they improved the tensioned membrane effect calculation model [21]. Liu et al. [22] used the Winkler elastic beam–foundation method to establish a calculation model for soil settlement between piles based on the membrane effect. The optimization method of bearing capacity of soil between piles is proposed. The rationality of this method is analyzed through field tests. Rao et al. [23] employed thin plate bending theory and the Winkler foundation model, solving for post-construction settlement using heavy trigonometric series solutions. Nevertheless, the relationship between subgrade reaction and settlement is not strictly linear in reality. Zhang et al. [24] employed the Winkler elastic foundation beam theory in their analysis, which considered the shear resistances at the top and bottom of the geosynthetic-reinforced platform. Semi-analytical solutions were proposed to quantify the effects of various factors, such as soil–beam interface resistance, pile stiffness, pile spacing and the elastic modulus of the foundation beam. Jiang et al. [25] introduced the Van Eekelen geosynthetic reinforcement model into the classical Chen Yunmin-improved Hewlett soil arching model, also accounting for the support from the inter-pile soil, to establish a load distribution calculation model for pile-supported geosynthetic-reinforced

embankments. However, this model still calculates the inter-pile soil reaction within the influence zone of the reinforcement based on the Winkler foundation model. Zhao et al. [26] analyzed the embankment and composite foundation within the equivalent reinforced zone of a single pile. By introducing a "soil column model" and an annular large-deflection thin plate to account for the embankment soil arching effect and the bending resistance of the geocell, respectively, and based on the layer-wise summation method, Hooke's law, and a hyperbolic model, they comprehensively considered pile bulging and pile–soil interface slip. This led to the establishment of a three-dimensional model considering the interaction between the embankment, geocell, and stone column composite foundation, ultimately deriving methods for calculating the pile–soil stress ratio and settlement. Cui et al. [27] fitted measured P-S curves into piecewise linear functions, using their slopes as subgrade reaction coefficients. They derived the fundamental theoretical equations for an elastic foundation beam with variable subgrade coefficients and solved them using the initial parameter method. However, the accumulation of errors increases significantly with multiple subgrade coefficients.

Meanwhile, numerical simulation technology has become an indispensable research tool in this field due to its unique advantages of replicating complex working conditions, enabling parametric analysis, and revealing internal mechanisms. In recent years, with the continuous improvement of constitutive theories and computational capabilities, research on numerical simulation has deepened, now allowing for the effective modeling of the mechanical behavior of pile-supported embankments. Numerical programs can also be used to define the load distribution mechanisms in geosynthetic-reinforced pile-supported embankments, accurately reproducing the stress mechanisms within the pile-supported system. Nobahar et al. [28] evaluated existing design methods for Geosynthetic-Reinforced Load Transfer Platforms in Pile-Supported Embankments (GLTP-PSE) through comprehensive three-dimensional finite element (FE) analysis. Ma et al. [29] established a Discrete Element Method (DEM) model for a full-scale pile-supported embankment in high-speed railways, considering the interaction among multiple piles. Using numerical simulation, they investigated the load transfer mechanism and soil arching process under the influence of self-weight, embankment pre-loading, and train-induced dynamic loads. The results indicated that under self-weight, a fully developed soil arch structure can be achieved with a sufficient embankment fill height, but the arch structure diminishes as the relative soil–pile displacement increases. Han et al. [30] conducted a numerical study considering three main influencing factors: fill height, geosynthetic tensile stiffness, and elastic modulus of the pile material. They investigated the pile–soil–geosynthetic interaction. The numerical results showed that the stress concentration ratio and maximum tension in the geosynthetic increase with greater embankment fill height, higher tensile stiffness of the geosynthetic, and increased elastic modulus of the pile material. Chen et al. [31] employed an elasto-plastic finite element method to analyze the distribution characteristics and dissipation process of excess pore water pressure in the foundation after instantaneous loading. They also studied the force in the reinforcement grid and the settlement characteristics of the embankment, analyzing the influence of pile length, pile spacing, and pile cap size on the pile load sharing ratio and embankment settlement.

Although the pile-supported geosynthetic-reinforced embankment technique has seen extensive application in engineering projects, its design principles remain relatively conservative. Given that major projects impose strict requirements on post-construction settlement, the accurate prediction of settlement has become imperative. Therefore, an in-depth investigation into the load-bearing mechanisms of these embankments and the development of a comprehensive design framework hold significant theoretical and practical importance.

## 2. Composition of Post-Construction Settlement

Post-construction settlement refers to the total settlement of the entire structural system occurring after the completion of the upper critical sections on a natural soft soil foundation. The total post-construction settlement (S) of a pile-supported geosynthetic-reinforced embankment comprises four components:

$$S = S_1 + S_2 + S_3 + S_4 \quad (1)$$

In this equation, $S_1$ denotes the compression of the overlying soil atop the platform layer; $S_2$ denotes the compression of the platform layer; $S_3$ denotes the compression occurring in the pile–soil reinforced zone; and $S_4$ denotes the compression of the subsoil beneath the pile ends.

In engineering practice, $S_1$ and $S_2$ are generally small and often negligible or can be roughly estimated. The computation of $S_4$ is well-established, for instance using the layer-wise summation method. In contrast, $S_3$ is considerably more challenging to determine due to the lack of a mature and systematic calculation approach. Thus, this paper focuses on the computational methodology for $S_3$.

Consider a scenario in a highway project with an infinitely long embankment and a rectangular pile arrangement, where the pile spacing is $l$ and the pile diameter is $d$. The unit cell of soil above four adjacent piles, indicated by the shaded area in Figure 2, is taken as the research object. The reinforced platform, composed of geosynthetics and a gravel layer, has a relatively small overall thickness $h$ and can be approximated as a thin plate. This plate deforms under the combined action of the overlying embankment, external loads, and the subgrade reaction from the underlying soil, as shown in Figure 2. It is generally assumed that the settlement induced by the embankment is uniform, and the load acting on the thin plate is also uniformly distributed, and can be calculated as follows.

$$q = \gamma H \quad (2)$$

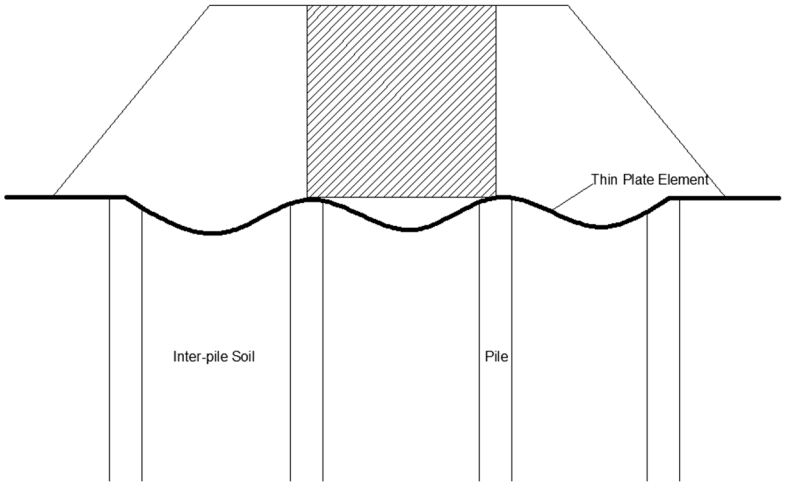


**Figure 2.** Deformation of the thin plate under embankment load.

In the equation, $\gamma$ signifies the unit weight of the embankment fill material; H refers to the total embankment height, which is the sum of the actual constructed height and the equivalent height accounting for any external surcharge loads.

Since the compressive deformation of the piles themselves is completed during the construction phase, the post-construction settlement in a sparsely piled design can be primarily

attributed to the inter-pile soil. Consequently, the post-construction settlement of the pile–soil improved zone ($S_3$) is defined by the maximum deflection of the geosynthetic element.

The geosynthetic material is usually thin, and the platform layer is composed of graded gravel. Together, the geosynthetic and the gravel layer form a composite mat with integral behavior. The thickness $h$ ranges from 0.2 to 0.5 m. Under typical conditions, the pile diameter $d$ is taken as 0.5 m and the pile spacing $l = 6d = 3$ m, satisfying $l/h \geq 5$. Thus, the mat unit can be approximately regarded as a thin plate.

## 3. Resolution of the Thin Plate Bending Problem

### *3.1. Fundamental Assumptions*

The analysis is based on the classical thin plate theory with the following core premises:

(1) The plate is modeled as a continuum with linear elastic, homogeneous, and isotropic material properties.

(2) The Kirchhoff hypothesis is adopted: fibers initially normal to the mid-surface remain straight, unstretched, and normal to the deformed mid-surface (the *xoy* plane in Figure 3).

(3) The stress components transverse to the mid-plane ($\tau_{xz}$, $\tau_{yz}$, $\sigma_z$) are negligible and do not contribute to the strain energy.

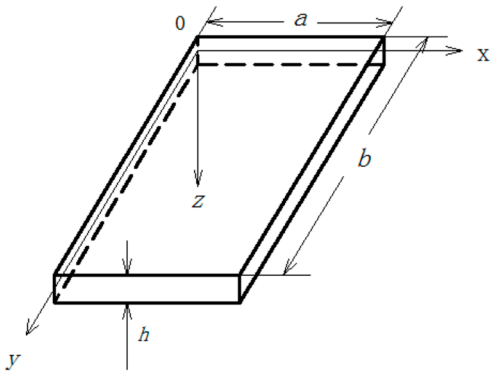


**Figure 3.** The thin plate simulated by the geosynthetic-reinforced platform.

### *3.2. Differential Equation for a Surface*

The governing differential equation for the deflection of a thin plate is given by [32]:

$$D\nabla^4 w = q - p \tag{3}$$

where

D denotes the flexural rigidity of the thin plate (unit: kN·m). The value of D can be obtained from the following equation:

$$D = Eh^3/12\left(1 - \nu^2\right) \tag{4}$$

$\nabla^4$ denotes the biharmonic operator (or double Laplace operator), and the value of $\nabla^4$ can be obtained from the following equation:

$$\nabla^4 = \frac{\partial^4}{\partial x^4} + 2\frac{\partial^4}{\partial x^2 \partial y^2} + \frac{\partial^4}{\partial y^4} \tag{5}$$

$w$ denotes the deflection of the plate;

E denotes the equivalent elastic modulus of the plate;

$\nu$ denotes Poisson's ratio of the plate;
$h$ denotes the thickness of the plate;
$q$ denotes the external load applied to the plate;
$p$ denotes the subgrade reaction (or soil counter-pressure) beneath the plate.

The platform is conventionally simulated using the linear Winkler foundation model. However, practical engineering experience has revealed its limitations in accuracy and rationality, and Zhuang et al. [33] observed the deformed geosynthetic in a piled embankment, as shown in Figure 4. While existing foundation models such as the Winkler model are concise in form, they neglect soil continuity and nonlinearity. The Pasternak model introduces a shear layer to account for load diffusion, and the Kerr model further refines soil stratification; however, these models remain linear in nature and fail to capture the nonlinear softening behavior of soft soils characterized by stiffness degradation under large deformations. To address this, the present study introduces a cubic correction term based on the Winkler model, establishing a foundation model that combines simplicity with the capability to describe nonlinear behavior. Therefore, this paper adopts a nonlinear model for the subgrade reaction modulus, expressed as

$$p(x,y) = K_1 w(x,y) - K_2 w^3(x,y) \tag{6}$$

where $K_1$ and $K_2$ denotes the parameters characterizing the subgrade reaction (unit: kN/m$^3$). The values of $K_1$ and $K_2$ are determined by the settlement back-calculated using the estimated settlement method for determining the subgrade reaction coefficient, as well as the foundation settlement obtained from elastic mechanics formulas.

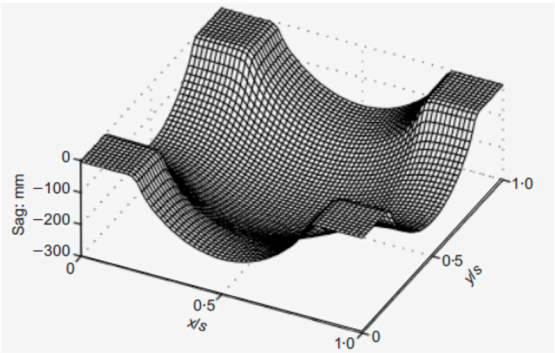


**Figure 4.** Vertical displacement of the three-dimensional deformed geosynthetic (Reprinted with permission from Ref. [33]. 2014, Thomas Telford Ltd., London, UK).

The substitution of Equation (6) into Equation (3) leads to

$$\nabla^4 w + \frac{K_1}{D} w - \frac{K_2}{D} w^3 = \frac{q}{D} \tag{7}$$

Equation (7) thus represents the governing differential equation describing the bending of a thin plate resting on a nonlinear foundation.

### *3.3. Calculation of Post-Construction Settlement*

For the case of a rectangular thin plate under simple support along its four edges, the boundary conditions are as shown in Figure 3, and its governing equation is given as follows:

$$(w)_{x=0,a} = 0,\ \left(\frac{\partial^2 w}{\partial x^2}\right)_{x=0,a} = 0;\ (w)_{y=0,b} = 0,\ \left(\frac{\partial^2 w}{\partial y^2}\right)_{y=0,b} = 0. \tag{8}$$

The double trigonometric series is taken as the solution to Equation (7):

$$w = \sum_{i=1}^{\infty}\sum_{j=1}^{\infty} A_{ij}\sin\frac{i\pi x}{a}\sin\frac{j\pi y}{b} \tag{9}$$

Equation (9) satisfies all the boundary conditions.

In order to determine the coefficients $A_{ij}$, Equation (9) is substituted into the governing differential equation for plate deflection, Equation (7), yielding:

$$\pi^4\sum_{i=1}^{\infty}\sum_{j=1}^{\infty}(\frac{i^2}{a} + \frac{j^2}{b})^2 A_{ij}\sin\frac{i\pi x}{a}\sin\frac{j\pi y}{b} + \frac{K_1}{D}\sum_{i=1}^{\infty}\sum_{j=1}^{\infty} A_{ij}\sin\frac{i\pi x}{a}\sin\frac{j\pi y}{b} - \frac{K_2}{D}\left(\sum_{i=1}^{\infty}\sum_{j=1}^{\infty} A_{ij}\sin\frac{i\pi x}{a}\sin\frac{j\pi y}{b}\right)^3 = \frac{q}{D} \tag{10}$$

Expand the $q/D$ of Equation (10) into a double trigonometric series:

$$\frac{q}{D} = \sum_{i=1}^{\infty}\sum_{j=1}^{\infty}\frac{q_{ij}}{D}\sin\frac{i\pi x}{a}\sin\frac{j\pi y}{b} \tag{11}$$

By applying the Fourier series expansion formula, it follows that:

$$\frac{q_{ij}}{D} = \frac{4}{ab}\sum_{i=1}^{\infty}\sum_{j=1}^{\infty}\int_0^a\int_0^b\frac{q}{D}\sin\frac{i\pi x}{a}\sin\frac{j\pi y}{b}dxdy \tag{12}$$

Hence:

$$\frac{q}{D} = \frac{4}{ab}\sum_{i=1}^{\infty}\sum_{j=1}^{\infty}\left[\int_0^a\int_0^b\frac{q}{D}\sin\frac{i\pi x}{a}\sin\frac{j\pi y}{b}\,dxdy\right]\sin\frac{\pi x}{a}\sin\frac{\pi y}{b} \tag{13}$$

Given the rapid convergence rate of the series, high precision is achieved even when only the fundamental term $i = j = 1$ is considered. Consequently, this term is adopted to reduce the computational effort.

Equation (10) is simplified into the following form:

$$\pi^4(\frac{1}{a^2} + \frac{1}{b^2})^2 A\sin\frac{\pi x}{a}\sin\frac{\pi y}{b} + \frac{K_1}{D}A\sin\frac{\pi x}{a} - \frac{K_2}{D}(A\sin\frac{\pi x}{a}\sin\frac{\pi y}{b})^3 = \frac{q}{D} \tag{14}$$

Similarly, Equation (13) is simplified as:

$$\frac{q}{D} = \frac{4}{ab}\left[\int_0^a\int_0^b\frac{q}{D}\sin\frac{\pi x}{a}\sin\frac{\pi y}{b}\,dxdy\right]\sin\frac{\pi x}{a}\sin\frac{\pi y}{b} \tag{15}$$

From the comparison of Equation (14) with Equation (15), it can be observed that:

$$\pi^4(\frac{1}{a^2} + \frac{1}{b^2})^2 A + \frac{K_1}{D}A - \frac{K_2}{D}A^3(\sin\frac{\pi x}{a}\sin\frac{\pi y}{b})^2 = \frac{4}{ab}\int_0^a\int_0^b\frac{q}{D}\sin\frac{\pi x}{a}\sin\frac{\pi y}{b}dxdy \tag{16}$$

In 1915, Galerkin published a paper in which he proposed a numerical analysis method, later known as the Galerkin method. This method involves selecting a finite number of trial functions, superimposing them, and requiring the weighted integral of the result over the solution domain and its boundaries to satisfy the original equation. This process yields a system of linear algebraic equations that are easy to solve and can inherently satisfy natural boundary conditions. By applying the variational principle of the functional corresponding to the equation, this method simplifies the problem of solving differential equations into solving a system of linear equations.

To determine coefficient A, the Galerkin method is employed. Both sides of Equation (16) are multiplied by the basis function $\sin\frac{\pi x}{a}$ and integrated over the domain

[0, a] to eliminate the $x$-dependence. Similarly, both sides of Equation (16) are multiplied by the basis function $\sin\frac{\pi y}{b}$ and integrated over [0, b] to eliminate the $y$-dependence. This process finally yields

$$4ab\pi^2(\frac{1}{a^2}+\frac{1}{b^2})^2A+\frac{4abK_1}{\pi^2D}A-\frac{16abK_2}{9\pi^2D}A^3=\frac{64\text{abq}}{\pi^4D} \tag{17}$$

After further simplification, the following can be obtained:

$$\pi^2(\frac{1}{a^2}+\frac{1}{b^2})^2A+\frac{K_1}{\pi^2D}A-\frac{4K_2}{9\pi^2D}A^3=\frac{16q}{\pi^4D} \tag{18}$$

Equation (18) is a cubic equation, and its solution can be obtained using Cardano's method. If the quadratic coefficient of a cubic equation is zero, i.e., the equation takes the form $x^3 + sx + t = 0$, it represents a special case of Cardano's formula, whose solution is given by

$$\begin{aligned} x_1&=\sqrt[3]{-\tfrac{t}{2}+\sqrt{\tfrac{t^2}{4}+\tfrac{s^3}{27}}}+\sqrt[3]{-\tfrac{t}{2}-\sqrt{\tfrac{t^2}{4}+\tfrac{s^3}{27}}}\\ x_2&=\sqrt[3]{-\tfrac{t}{2}+\sqrt{\tfrac{t^2}{4}+\tfrac{s^3}{27}}}c+\sqrt[3]{-\tfrac{t}{2}-\sqrt{\tfrac{t^2}{4}+\tfrac{s^3}{27}}}c^2\\ x_3&=\sqrt[3]{-\tfrac{t}{2}+\sqrt{\tfrac{t^2}{4}+\tfrac{s^3}{27}}}c^2+\sqrt[3]{-\tfrac{t}{2}-\sqrt{\tfrac{t^2}{4}+\tfrac{s^3}{27}}}c \end{aligned} \tag{19}$$

where the value of c can be obtained from the following equation:

$$c=\frac{-1+\sqrt{3}i}{2} \tag{20}$$

The discriminant is given by the following equation:

$$\Delta=\frac{t^2}{4}+\frac{s^3}{27} \tag{21}$$

When the discriminant is greater than zero, the equation has one real root and two complex roots. When the discriminant is equal to zero, the equation has three real roots, two of which are identical. When the discriminant is less than zero, the equation has three distinct real roots.

Once coefficient A has been obtained, it can be substituted into Equation (18) to yield

$$w=A\sin\frac{\pi x}{a}\sin\frac{\pi y}{b} \tag{22}$$

When the thin plate is subjected to a uniformly distributed load, i.e., $q(x, y) = q_0$, the following can be inferred based on the load-bearing mechanism of the pile-supported geosynthetic-reinforced embankment:

$$q_0=\frac{q}{1+m(n-1)}=\frac{\gamma H}{1+m(n-1)} \tag{23}$$

where $m$ denotes the area replacement ratio; $n$ denotes the pile–soil stress ratio.

For the case of a uniformly distributed load under an embankment and a square thin plate ($a = b = l$), substituting these conditions into Equation (22) and setting $x = l/2$, $y = l/2$ yields the deflection at the center of the plate. This deflection represents the maximum deformation of the geosynthetic unit, i.e., the post-construction settlement $w_{\max}$ of the pile–soil improved zone:

$$w_{\max}=A \tag{24}$$

Due to the numerous assumptions inherent in the study of pile-supported geosynthetic-reinforced embankments and the complex variability of actual engineering conditions, the post-construction settlement of the pile–soil improved zone is as follows:

$$S_3 = m_s w_{max} = m_s A \quad (25)$$

where $m_s$ denotes the empirical correction coefficient derived from actual project statistics.

### *3.4. Case Study*

A subgrade project [23] employed the ground improvement method of a pile-supported geosynthetic-reinforced embankment. The unit weight of the compacted embankment fill was taken as $\gamma$ = 20 kN/m$^3$, and the total equivalent embankment height after load conversion was H = 5 m. The cement deep mixing piles had a length $h_p$ = 12 m, diameter $d$ = 0.5 m, and spacing $l = 6d$ = 3 m, arranged in a square pattern, resulting in an area replacement ratio $m = \pi d^2/(4l^2)$ = 2.18%. The characteristic bearing capacity of the natural soft soil between piles was $f_k$ = 80 kPa, and the subgrade reaction coefficients were taken as $K_1$ = 5870 kN/m$^3$ and $K_2$ = 2,174,000 kN/m$^3$.

The reinforcement material was geogrid, with a reinforced platform thickness $h$ = 0.3 m. The measured composite's Poisson ratio of the reinforced platform was $\nu$ = 0.15, and the composite elastic modulus was E = $10^5$ kN/m$^2$, yielding a calculated bending stiffness of the reinforcement D = 230 kN·m.

Taking the comprehensive empirical correction coefficient $m_s$ =1 and substituting the above values into Equation (18), the calculated result is $S_3$ = 0.0201 m = 20.1 mm. This value is closely aligned with field measurements and results obtained from other approximate methods.

### *3.5. Finite Element Simulation*

For the purpose of validating the proposed nonlinear foundation model, a finite element analysis was conducted to simulate the post-construction settlement of inter-pile soil. The numerical results were then benchmarked against the theoretical predictions for verification.

#### 3.5.1. Model Establishment and Boundary Conditions

The model employs an implicit solution method for static analysis. To maintain computational accuracy while effectively controlling model scale and improving solution efficiency, several rational simplifications were implemented during geometric modeling. Based on structural and loading symmetry, a three-dimensional axisymmetric model was constructed. Furthermore, to streamline computation and facilitate a standardized comparison of results, a unit length of 1 m in the out-of-plane direction (thickness) was adopted as the representative analysis domain. The finite element model and its corresponding mesh configuration are presented in Figure 5.

In the vertical direction ($z$-axis), representing foundation depth, the total soil height was set to 12 m, with the bottom boundary modeled as a rigid, impermeable layer assumed to be non-deformable and waterproof. To minimize the interference of boundary constraints on the stress–strain field of the subgrade-foundation system (i.e., to eliminate boundary effects), the horizontal extent of the soil beneath the embankment was set to no less than three times the embankment length, following Saint-Venant's principle and common engineering practice [28]. Specifically, with a base width of 7.5 m for the half-width embankment, the total length of the underlying soil in the horizontal $x$ direction was extended to 28.5 m to ensure adequate development of the stress and displacement fields, thereby yielding more realistic simulation results.

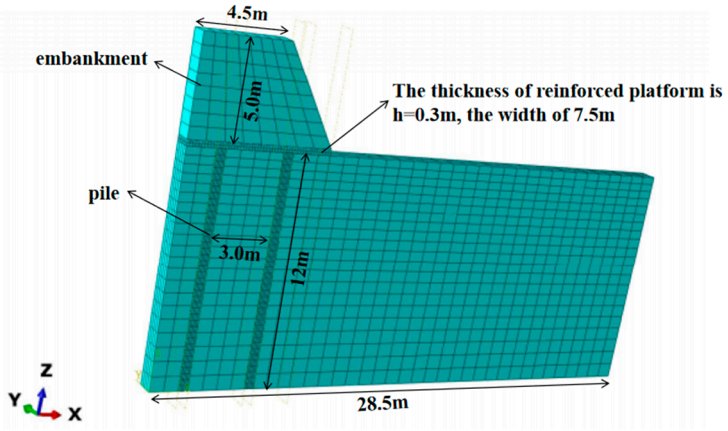


**Figure 5.** Finite element mesh.

The boundary conditions were defined as follows. The bottom surface of the model ($z$ = 0 plane) was treated as a fully fixed support, restricting all nodal displacements in the $x$, $y$, and $z$ directions. On the two symmetric boundaries, normal displacement constraints were applied: the symmetry plane along the embankment axis ($x$ = 0 plane) had its $x$-direction displacement constrained to enforce symmetric conditions, and the outer boundary ($x$ = 28.5 m plane) also had its $x$-direction displacement fixed to simulate the restraining effect of the far-field soil, while displacements in other directions on these surfaces remained unconstrained. Finally, on the two vertical surfaces in the thickness direction ($y$ = 0 m and $y$ = 1 m planes), y-direction displacements were restricted with no constraints imposed on the remaining degrees of freedom.

### 3.5.2. Model Meshing and Computational Parameters

The embankment fill and foundation soil were simulated using an ideal elastoplastic model based on the Mohr–Coulomb failure criterion, which incorporates five parameters: effective cohesion $c'$, effective internal friction angle $\varphi'$, dilation angle $\psi$, elastic modulus E, and Poisson's ratio $\nu$. To simplify the analysis, material dilation was neglected by setting the dilation angle to 0°. The lateral earth pressure coefficient of the foundation soil was calculated as $1 - \sin \varphi'$, yielding a value of 0.658 in this model. The piles were modeled as linear elastic materials with an elastic modulus of 20 GPa and a Poisson's ratio of 0.2. The computational parameters for the Mohr–Coulomb model of the foundation soil were determined by converting the characteristic bearing capacity of the natural soft soil between piles. All components were discretized using 8-node linear brick elements (C3D8). The approximate global size of the embankment fill was set to 0.75, which was divided into 64 units. The approximate global size of the foundation soil was 0.8, and the top and bottom of the pile position were densely planted according to the number, which was divided into 3948 units. The approximate global size of the pile was 0.3, and the pile top and pile body were appropriately densely seeded according to the number. The number of units in the size control was set to 6, and a total of 520 units were divided. The pile–soil interface was simulated using zero-thickness contact elements (surface-to-surface contact). These elements represent the interaction between two surfaces without possessing material properties of their own, and are used to define force transmission, separation, and penetration behavior between contacting surfaces [29].

The reinforced platform was modeled as linear elastic, and contact elements were inserted at both the upper and lower interfaces with the embankment and foundation soil. The contact behavior follows the Mohr–Coulomb failure criterion, with the interface friction angle set to be equal to that of the foundation soil and the interface cohesion taken as zero. This part of the model was discretized with 8-node linear brick elements with

reduced integration and hourglass control (C3D8R). The approximate global size of the reinforced platform is 0.15, which is divided into 700 units. The static general analysis step is used in the loading stage; the maximum increment step is 100, and the initial increment step is 0.05. The model parameters are summarized in Table 1, and the overall geometry and discretization are shown in Figure 5. During meshing, local refinement was applied to the reinforced platform and the piles, particularly in the contact region between them, to achieve a finer mesh density. This helps prevent stress concentration and simulation interruption caused by excessive mesh distortion during computation, thereby ensuring numerical stability and accuracy.

**Table 1.** Parameters for finite element analysis.

| Material | Model | $c'$/kPa | $\varphi'$/(°) | Ψ/(°) | *E*/MPa | $\nu$ | $\gamma$/(kN/m$^3$) |
|---|---|---|---|---|---|---|---|
| Embankment Fill | Mohr–Coulomb | 10 | 30 | 0 | 10 | 0.3 | 20 |
| Reinforced Platform | Linear elastic | - | - | - | 100 | 0.15 | 25 |
| Foundation Soil | Mohr–Coulomb | 5 | 20 | 0 | 10 | 0.35 | 22 |
| Pile | Linear elastic | - | - | - | $20 \times 10^6$ | 0.2 | 25 |

#### 3.5.3. FEM Results

Figure 6 illustrates the contour of settlement displacement (where U3 denotes the displacement along the *Z*-axis, i.e., the settlement) at the end of the analysis. Figure 7 presents the settlement of the inter-pile soil obtained from the finite element analysis following the aforementioned modeling procedure. Consistent with the correspondence established earlier, the deformation of the reinforced platform is taken to represent the settlement of the inter-pile soil. During the simulation, the reinforced platform elements remain in continuous contact with the underlying soil elements. Accordingly, the *z*-direction displacement at the nodal point of the element located at the center of the reinforced slab (or the center of the foundation soil between two piles) is selected as the representative value of the inter-pile soil settlement in the output results.

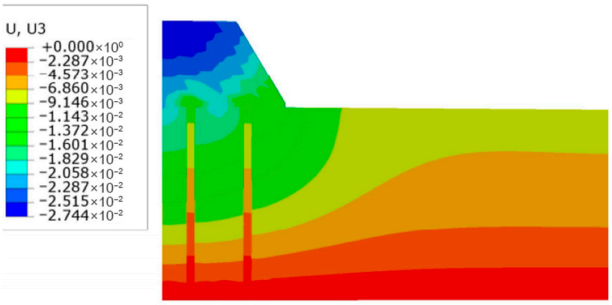


**Figure 6.** Contour of settlement displacement.

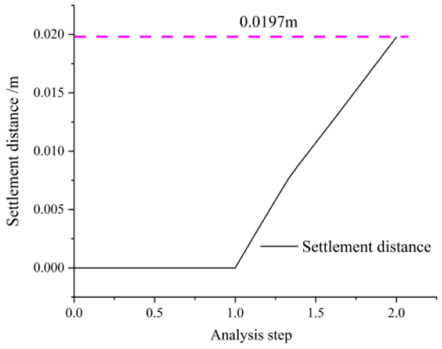


**Figure 7.** Settlement of inter-pile soil.

The irregular pattern of the settlement contours in Figure 6 is caused by the deformation incompatibility due to the stiffness contrast between the piles and the soil, together with the numerical noise inherent in solving strongly nonlinear problems in ABAQUS 2023. This phenomenon is particularly pronounced around the piles, where stress concentration and contact state changes occur simultaneously.

As shown in Figure 7, the finite element simulation result indicates a final post-construction settlement of 19.7 mm. This value differs by only 0.4 mm from the result obtained using the nonlinear model calculation (20.1 mm), with a relative error of less than 2%, thereby validating the correctness and rationality of the proposed computational method. It is worth noting that the horizontal segment in Figure 7 corresponds to the geostatic equilibrium phase (geostatic analysis step) in the finite element software, during which the soil develops its initial stress field without generating net settlement displacement.

## 4. Analysis of Factors Influencing Post-Construction Settlement

Numerous parameters influence the post-construction settlement $S_3$ of pile-supported geosynthetic-reinforced embankments. This paper focuses on investigating the effects of the bending stiffness D, the subgrade reaction coefficient $K_1$, the pile spacing $l$, and the total embankment height H (after surcharge conversion) on $S_3$.

The value ranges for these parameters are determined based on relevant engineering data and practical experience: the bending stiffness is taken as $100 < D < 2000$ kN·m, the subgrade reaction coefficient as $5000 < K_1 < 9000$ kN/m$^3$, the pile spacing as $1.5 < l < 3.5$ m, and the total converted embankment height as $3.5 < H < 5.5$ m.

### *4.1. Influence of the Equivalent Embankment Height (H) on Post-Construction Settlement ($S_3$)*

The bending stiffness D was assigned values of 100, 200, 500, 1000, and 2000 kN·m, while varying the embankment height H. With all other known parameters from the case study in Section 3.4 remaining unchanged, the results were substituted into Equation (18) and plotted in Figure 8. Similarly, the subgrade reaction coefficient $K_1$ was varied at intervals of 1000 kN/m$^3$ with changes in embankment height H, while keeping other parameters constant, and the results are presented in Figure 9. Likewise, the pile spacing $l$ was varied at intervals of 0.5 m, and the corresponding results are shown in Figure 10.

As shown in Figures 8–10, the settlement $S_3$ increases with the embankment height H when $H < 4.5$ m. However, when $H > 4.5$ m, $S_3$ remains nearly constant. This stabilization occurs because the maximum deflection of the geosynthetic, which defines the value of $S_3$, is reached when the inter-pile soil attains its ultimate bearing capacity.

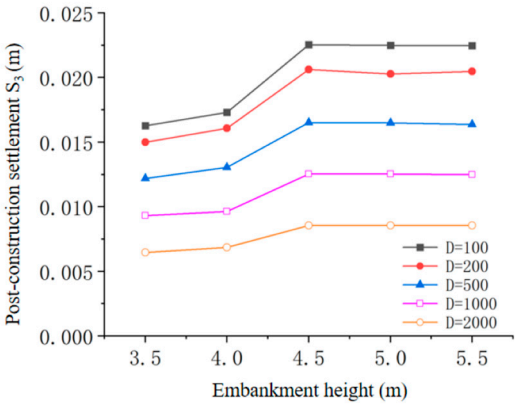


**Figure 8.** $S_3$-H curve at different bending stiffnesses.

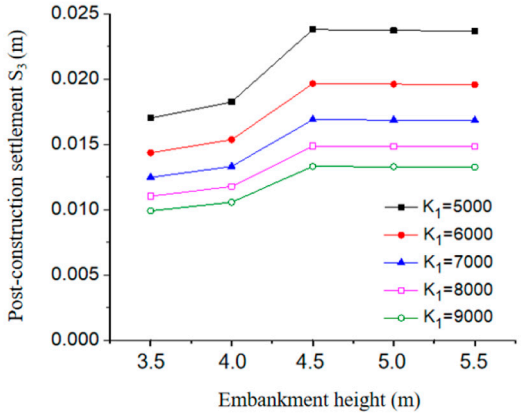


**Figure 9.** $S_3$-H curve at different coefficients of subgrade reaction.

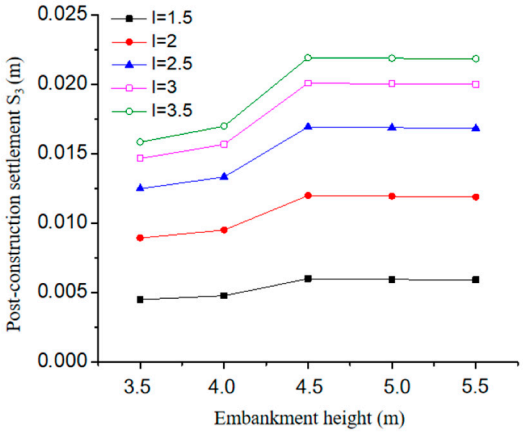


**Figure 10.** $S_3$-H curve at different pile spacings.

### *4.2. Influence of Bending Stiffness (D) on Post-Construction Settlement (S3)*

The subgrade reaction coefficient $K_1$ was assigned values at intervals of 1000 kN/m$^3$ while systematically varying the bending stiffness D. With all other known parameters from the case study in Section 3.4 remaining unchanged, the results were computed using Equation (18) and are plotted in Figure 11. Similarly, the pile spacing *l* was varied at 0.5 m intervals while changing the bending stiffness D, with other parameters held constant. The corresponding results obtained from Equation (18) are shown in Figure 12. Likewise, the converted embankment height H was assigned values at 0.5 m intervals, and the resulting responses are presented in Figure 13.

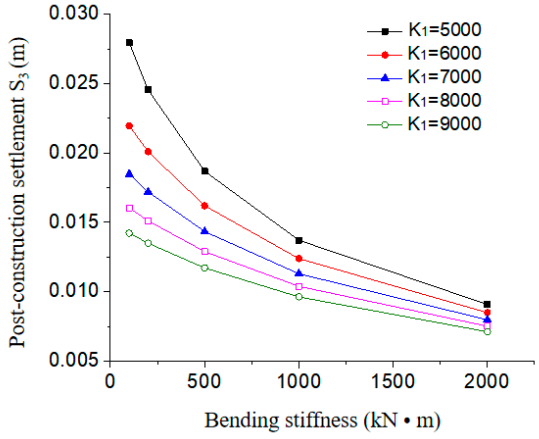


**Figure 11.** $S_3$-D curve at different coefficients of subgrade reaction.

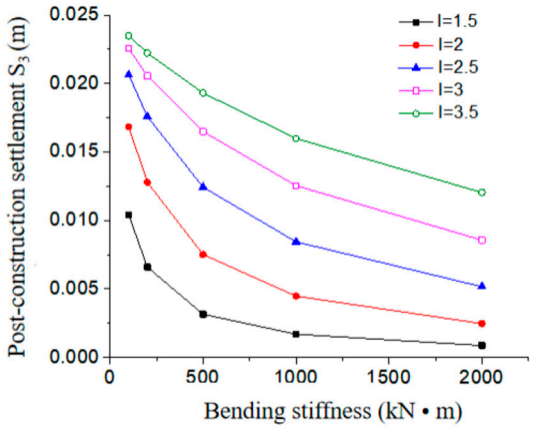


**Figure 12.** $S_3$-D curve at different pile spacings.

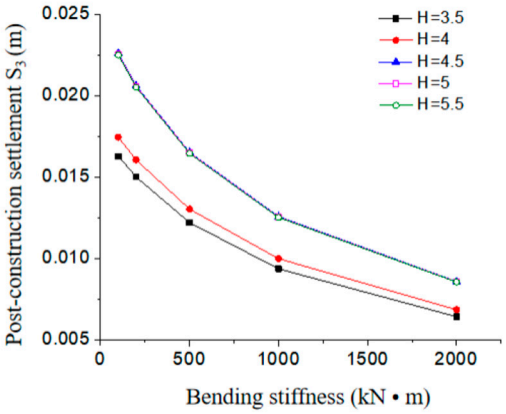


**Figure 13.** $S_3$-D curve at different embankment heights.

As shown in Figures 11–13, $S_3$ decreases with increasing bending stiffness D. Moreover, when D reaches higher values, its influence on the post-construction settlement $S_3$ becomes less pronounced. This phenomenon is attributed to the increased modulus, which causes the thin plate to demonstrate rigid-body characteristics with consequently diminished bending deformation.

### *4.3. Influence of Subgrade Reaction Coefficient $K_1$ on Post-Construction Settlement ($S_3$)*

The bending stiffness D was assigned values of 100, 200, 500, 1000, and 2000 kN·m, while varying the subgrade reaction coefficient $K_1$. With all other known parameters from the case study in Section 3.4 remaining unchanged, the results were computed using Equation (18) and are plotted in Figure 14. Similarly, the pile spacing *l* was varied at 0.5 m intervals while changing the subgrade reaction coefficient $K_1$, and the corresponding results calculated from Equation (18) are shown in Figure 15. Likewise, the embankment height H was assigned values at 0.5 m intervals while varying the subgrade reaction coefficient $K_1$, with the resulting responses presented in Figure 16.

As shown in Figures 14–16, the post-construction settlement $S_3$ decreases as the subgrade reaction coefficient $K_1$ increases. Moreover, when $K_1$ reaches relatively high values, its influence on $S_3$ becomes less pronounced. The enhancement of the subgrade reaction coefficient essentially improves the load-bearing and deformation coordination capability of the inter-pile soil, resulting in an optimized load transfer and deformation behavior of the whole system, and consequently a decrease in post-construction settlement.

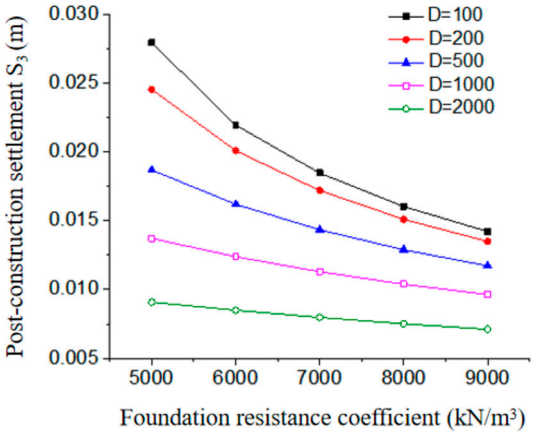


**Figure 14.** $S_3$-$K_1$ curve at different bending stiffnesses.

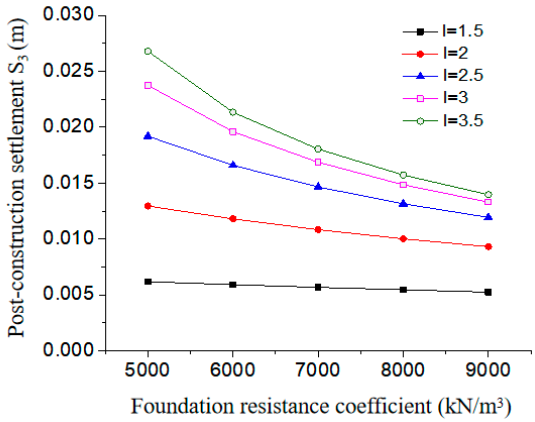


**Figure 15.** $S_3$-$K_1$ curve at different pile spacings.

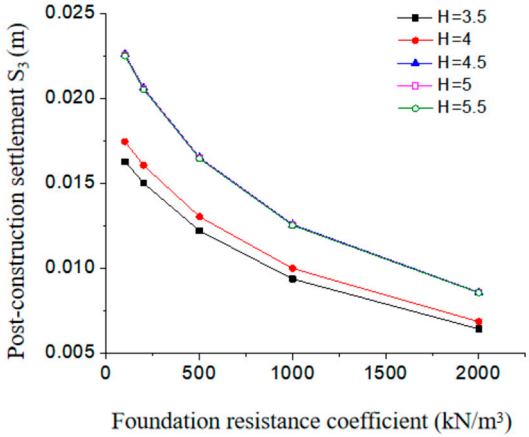


**Figure 16.** $S_3$-$K_1$ curve at different embankment heights.

### *4.4. Influence of Pile Spacing (L) on Post-Construction Settlement ($S_3$)*

The bending stiffness D was assigned values of 100, 200, 500, 1000, and 2000 kN·m, while varying the pile spacing *l*. With all other known parameters from the case study in Section 3.4 held constant, the results were computed using Equation (18) and are plotted in Figure 17. Similarly, the subgrade reaction coefficient $K_1$ was varied at intervals of 1000 kN/m$^3$ (while concurrently adjusting the pile spacing *l*), and the corresponding results calculated from Equation (18) are shown in Figure 18. Likewise, the embankment height H was assigned values at 0.5 m intervals while varying the pile spacing *l*, with the resulting responses presented in Figure 19.

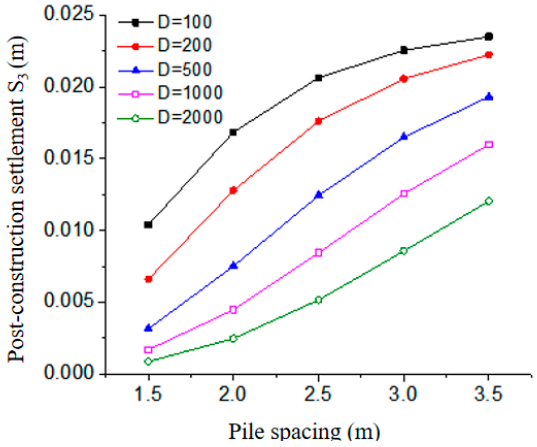


**Figure 17.** $S_3$-*l* curve at different bending stiffnesses.

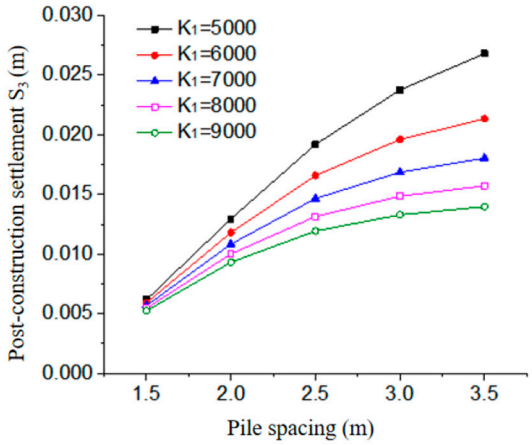


**Figure 18.** $S_3$-*l* curve at different coefficients of subgrade reaction.

Figures 17–19 indicate that the post-construction settlement $S_3$ grows as the pile spacing *l* increases. For $l > 3$ m, the sensitivity of $S_3$ to changes in *l* decreases, and the settlement approaches a constant value. The primary mechanism is that wider pile spacings shift more of the embankment load onto the soft inter-pile soil, which in turn generates greater settlement.

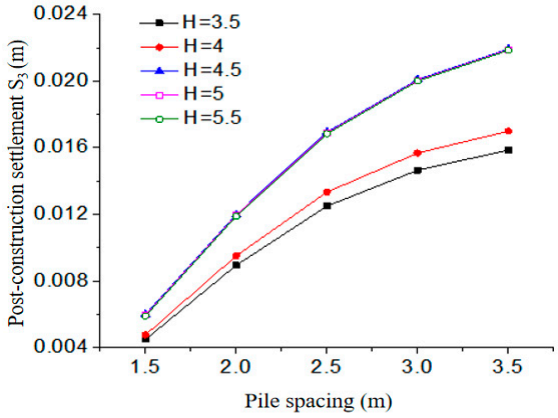


**Figure 19.** $S_3$-*l* curve at different embankment heights.

### *4.5. Sensitivity Analysis of Influencing Parameters*

The variable $\rho$ is defined to quantify the degree of parameter influence, and its expression is given by

$$\rho = \frac{\left| S_3' - S_3 \right|}{S_3} \tag{26}$$

where $S_3$ is the post-construction settlement (20.1 mm) under baseline parameter values from Section 3.4, and $S_3'$ is the settlement calculated with varied parameters.

To compare the degree of influence of the three parameters (note: the embankment height H is excluded from this comparison due to the abrupt change in post-construction settlement observed on either side of H = 4.5 m), the parameters $l$, $K_1$, and D were varied proportionally while keeping other parameters unchanged. The variation ranges for all parameters were set according to the common practical ranges established in the case study of Section 3.4. The computational results are summarized in Table 2 and graphically represented in Figure 20.

**Table 2.** The value of $\mu$ when parameters are varied.

| Influencing Parameters | $K_1$ (kN/m$^3$) | $l$ (m) | D (kN·m) |
|---|---|---|---|
| parameter decreased by 40% | --- | 0.5238 | 0.0838 |
| parameter decreased by 30% | 0.5297 | 0.3487 | 0.0614 |
| parameter decreased by 20% | 0.2738 | 0.2000 | 0.0399 |
| parameter decreased by 10% | 0.1152 | 0.0848 | 0.0195 |
| parameter increased by 10% | 0.0903 | 0.0614 | 0.0185 |
| parameter increased by 20% | 0.1636 | 0.1048 | 0.0364 |
| parameter increased by 30% | 0.2255 | 0.1357 | 0.0534 |
| parameter increased by 40% | 0.2778 | 0.1581 | 0.0698 |

Note: "---" indicates that this case was not calculated (the corresponding subsoil is too soft and uncommon in practice).

As observed from Figure 20, when the three parameters vary within their common ranges of engineering practice, the subgrade reaction coefficient $K_1$ exerts the most pronounced influence on the post-construction settlement $S_3$, followed by the pile spacing $l$, while the bending stiffness D demonstrates the least effect.

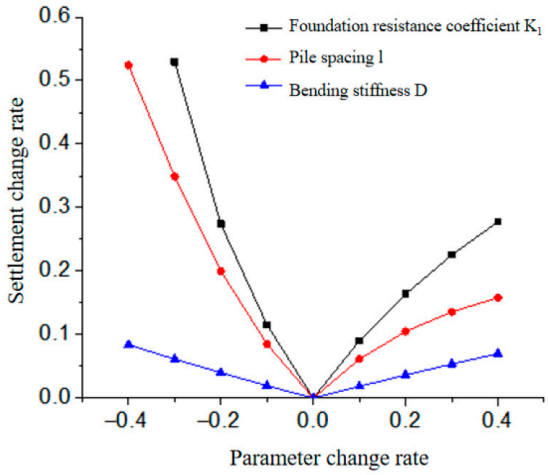


**Figure 20.** Settlement variation rate curves with parametric variation rate.

## 5. Conclusions

(1) The post-construction settlement of the pile–soil improved zone in a pile-supported geosynthetic-reinforced embankment was calculated using thin plate bending theory and a nonlinear foundation model. By considering the influence of the vertical

resistance of the inter-pile soil on the post-construction settlement, an analytical expression for the post-construction settlement of the pile–soil improved zone was derived and validated through an engineering case study.

(2) The settlement of the pile-supported geosynthetic-reinforced embankment was simulated via finite element analysis, employing implicit static analysis with three analysis steps and incorporating the built-in elastoplastic Mohr–Coulomb model. The final simulation result of 19.7 mm differed by only 0.4 mm from the result calculated in this study, verifying the accuracy of the proposed computational method. Furthermore, compared with the analytical solution obtained by Rao et al. [23] based on the Winkler linear foundation model and thin plate theory (22 mm), the result of the proposed model (20.1 mm) is closer to the finite element result (19.7 mm), further demonstrating the improved accuracy of the nonlinear model with the cubic correction term.

(3) The post-construction settlement $S_3$ consistently increases with larger pile spacing $l$ or with reductions in the subgrade reaction coefficient $K_1$ and bending stiffness D. When the embankment height is below the critical value converted from the maximum bearing capacity of the inter-pile soil, the post-construction settlement increases with H. However, when H exceeds this critical value, the growth rate of post-construction settlement significantly slows down and tends to stabilize.

(4) Based on proportional variations around the values adopted in the present engineering case study, it is observed that within common practical ranges, the subgrade reaction coefficient $K_1$ has the most pronounced influence on the post-construction settlement $S_3$, followed by the pile spacing $l$, while the bending stiffness D exhibits the least effect. Therefore, to reduce post-construction settlement, it is essential to strictly control the load (e.g., by using lightweight fill or reducing embankment height), increase the subgrade reaction coefficient (e.g., by improving the soft inter-pile soil), appropriately reduce pile spacing, and moderately increase bending stiffness (e.g., by selecting high-quality reinforcement materials or increasing the platform thickness). This ranking of parameter importance can serve as a valuable reference for the determination of relevant design values in current design guidelines.

(5) The proposed model is applicable to pile-supported geosynthetic-reinforced embankments in soft soil areas, where the reinforced platform satisfies $l/h \geq 5$ or acts as a rigid platform.

(6) The sensitivity analysis employed in this study is a local sensitivity analysis, considering only the effect of a single parameter varying around its baseline value, without capturing interactions between parameters. For more comprehensive global sensitivity analysis, methods such as orthogonal experimental design can be applied.

(7) It should be noted that the various approximations and assumptions made in the derivation may lead to discrepancies between calculated results and field measurements. The question of how to validate and calibrate the proposed analytical expressions through engineering practice will be a key focus of future research. In addition, this study has not fully considered complex factors such as creep effects; incorporating creep into long-term settlement prediction is also an area that requires further improvement.

**Author Contributions:** Conceptualization, C.S. and J.Q.; methodology, C.S.; software, L.W., X.Z. and D.C.; validation, Y.S. and X.Y.; formal analysis, C.S., J.Q., G.L., L.W. and H.L.; data curation, X.Y.; writing—original draft preparation, H.L.; writing—review and editing, C.S., J.Q. and S.X.; visualization, X.Z. and D.C.; supervision, C.S., J.Q. and Y.S.; project administration, C.S., Y.S. and G.L.; funding acquisition, C.S. All authors have read and agreed to the published version of the manuscript.

**Funding:** This research was funded by Kashi University under grant number (2023) 2871.

**Data Availability Statement:** All data are available upon request from the corresponding author.

**Conflicts of Interest:** The authors declare no conflicts of interest.

## References


1. Pan, G.; Liu, X.; Yuan, S.; Wang, Y.; Sun, D.; Feng, Y.; Jiang, G. A Field Study on the Arching Behavior of a Geogrid-Reinforced Floating Pile-Supported Embankment. *Transp. Geotech.* **2022**, *37*, 100795. [CrossRef]
2. Cui, X.; Zhuang, Y.; Ning, S.; Wang, K. An analytical method to calculate the settlement of reinforced piled embankment considering three-dimensional deformed geogrid. *Eur. J. Environ. Civ. Eng.* **2022**, *26*, 3648–3661. [CrossRef]
3. Borges, J.L. Geosynthetic-Reinforced and Stone Column-Supported Embankments: Numerical and Stability Study. *Geotech. Geol. Eng.* **2023**, *42*, 1933–1955. [CrossRef]
4. Xiong, C.; Guo, Z.; Xing, Z.; Zheng, J.; Liu, P.; Chen, F.; Jiang, X.; Li, X.; Chen, Y. An analytical solution for settlement of pile-supported reinforced low embankment considering lateral friction along pile shaft. *Transp. Geotech.* **2025**, *50*, 101478. [CrossRef]
5. Gao, J.; Xu, H.; Qian, J.; Gong, Y.; Zhan, L.; Chen, P. Settlement Behavior of Soft Subgrade Reinforced by Geogrid-Encased Stone Column and Geocell-Embedded Sand Cushion: A Numerical Analysis. *Adv. Civ. Eng.* **2020**, *2020*, 8874520. [CrossRef]
6. Guo, X.; Pham, T.A.; Dias, D. Probabilistic analysis of geosynthetic-reinforced and pile-supported embankments. *Comput. Geotech.* **2022**, *142*, 104595. [CrossRef]
7. Guo, W.; Huang, Y.; Ren, Y. A simplified analysis of a configuration of geosynthetic reinforcement in GRPS embankments. *Geotext. Geomembr.* **2023**, *51*, 2–16. [CrossRef]
8. Pham, T.A. Design and analysis of geosynthetic-reinforced and floating column-supported embankments. *Int. J. Geotech. Eng.* **2022**, *16*, 1276–1292. [CrossRef]
9. Pham, T.A.; Tran, Q.-A.; Villard, P.; Dias, D. Numerical Analysis of Geosynthetic-Reinforced and Pile-Supported Embankments Considering Integrated Soil-Structure Interactions. *Geotech. Geol. Eng.* **2023**, *42*, 185–206. [CrossRef]
10. Zhang, D.; Yang, G.; Li, T.; Xu, P.; Su, P. Model tests study of multi-layer geosynthetic-reinforced pile-supported embankments and evaluation of analytical design models. *Transp. Geotech.* **2025**, *51*, 101521. [CrossRef]
11. Xie, M.; Li, L.; Cao, W.; Zheng, J.; Dong, X. Centrifugal and numerical modeling of embankment widening over soft soils treated by pile-supported geosynthetic-reinforced soil wall. *Acta Geotech.* **2022**, *18*, 829–841. [CrossRef]
12. Feng, S.; Xu, R.; Yu, J.; Zhang, C.; Cheng, K. Field Monitoring of Geogrid-Reinforced and Pile-Supported Embankment at Bridge Approach. *Int. J. Geosynth. Ground Eng.* **2021**, *7*, 2. [CrossRef]
13. Wang, X.; Wang, X.; Yang, G.; Pu, C.; Jin, J. Field Test on Deformation Characteristics of Pile-Supported Reinforced Embankment in Soft Soil Foundation. *Sustainability* **2022**, *14*, 7805. [CrossRef]
14. Wang, G.; Zhang, X.; Liu, X.; Chang, Z.; Liu, Z. Large-scale Field Tests of the Performance of Geogrid-reinforced Piled Embankment over Soft Soil. *KSCE J. Civ. Eng.* **2023**, *28*, 655–672. [CrossRef]
15. Zhou, S.; Wang, B.; Shan, Y. Review of research on high-speed railway subgrade settlement in soft soil area. *Railw. Eng. Sci.* **2020**, *28*, 129–145. [CrossRef]
16. He, Z.; Wang, P.; Liu, Y. Cumulative deformation prediction and microstructure change of coarse-grained soil under cyclic loading. *Soil Dyn. Earthq. Eng.* **2023**, *173*, 108136. [CrossRef]
17. Zhang, J.; Zheng, J.; Ma, Q. Mechanical performance of biaxial reinforcement composite foundation under embankment loads. *Chin. J. Geotech. Eng.* **2010**, *32*, 1392–1398. (In Chinese)
18. Zheng, J.; Wang, X.; Chen, B. Pile-soil stress ratio of piled composite ground under geosynthetics-reinforced embankment. *J. HU ST (Urban Sci. Ed.)* **2007**, *24*, 5–8. (In Chinese)
19. Zhao, M.; Liu, D.; Zhang, L. Calculation for pile-soil stress ratio of two-direction reinforced composite foundation. *Eng. Mech.* **2009**, *26*, 176–181. (In Chinese)
20. Zhao, M.; Zhang, Y.; Liu, M.; Xiao, Y. Deformation Analysis of Geocell Reinforcement Considering Vertical and Horizontal Coupling Deformation. *J. Hunan Univ. (Nat. Sci.)* **2019**, *46*, 89–99. (In Chinese)
21. He, Z.; Luo, S.; Wang, P. Improved calculation model of load sharing of pile-supported reinforced cushion embankment. *J. Cent. South Univ. (Sci. Technol.)* **2024**, *55*, 2286–2294. (In Chinese)
22. Liu, Z.; Zhang, A.; Xu, J.; Zhou, C.; Zhang, L. Calculation model and bearing capacity optimization method for the soil settlement between piles in geosynthetic-reinforced pile-supported embankments based on the membrane effect. *PLoS ONE* **2021**, *16*, e0256190. [CrossRef] [PubMed]
23. Rao, W.; Jiang, H.; Hou, Q. Deformation of sheet plate due to residual settlement of pile-net composite foundation. *J. Hydraul. Eng.* **2002**, *4*, 23–27. (In Chinese)
24. Zhang, L.; Zhao, M.; Hu, Y.; Zhao, H.; Chen, B. Semi-analytical solutions for geosynthetic-reinforced and pile-supported embankment. *Comput. Geotech.* **2012**, *44*, 167–175. [CrossRef]

25. Jiang, Y.; He, N.; Qian, Y.; Zhang, Z.; Wang, Y. Modified load sharing calculation model of geosynthetic-reinforced and pile-supported embankments. *Hydro-Sci. Eng.* **2023**, 131–139. (In Chinese) [CrossRef]
26. Zhao, M.; Liu, M.; Ma, B.; Long, J. Calculation for stress concentration ratio and settlement of bidirectional reinforced composite foundation consisting of geocell mattress and stone column under embankment. *China J. Highw. Transp.* **2016**, *29*, 1–10. (In Chinese)
27. Cui, Y.; Jiang, Y.; Bao, P. Computing method of elastic foundation beam with variable bedding value and its application. *Rock Soil Mech.* **2003**, *24*, 565–567. (In Chinese)
28. Nobahar, M.; Abu-Farsakh, M.Y.; Izadifar, M. Evaluating the mechanisms and performance of Geosynthetic-Reinforced Load Transfer Platform of pile-supported embankments design methods. *Geotext. Geomembr.* **2024**, *52*, 1112–1133. [CrossRef]
29. Ma, Y.; Hu, J.; Xue, D.; Lü, X. Investigating soil arching in pile-supported embankments through physical experiments and DEM simulations. *Geotech. Geol. Eng.* **2024**, *42*, 3857–3875. [CrossRef]
30. Han, J.; Gabr, M.A. Numerical Analysis of Geosynthetic-Reinforced and Pile-Supported Earth Platforms over Soft Soil. *J. Geotech. Geoenviron. Eng.* **2002**, *128*, 44–53. [CrossRef]
31. Chen, R.P.; Jia, N.; Chen, Y.M. Mechanism and Settlement Analysis of pile-supported and Geogrid-Reinforced Embankments. *Chin. J. Rock Mech. Eng.* **2005**, *24*, 4358–4367.
32. Xu, Z. *Elastic Mechanics (Part II)*; Higher Education Press: Beijing, China, 1979. (In Chinese)
33. Zhuang, Y.; Ellis, E. Finite-element analysis of a piled embankment with reinforcement compared with BS 8006 predictions. *Géotechnique* **2014**, *64*, 910–917. [CrossRef]